AGU ADVANCING EARTH AND SPACE SCIENCE

Earth and Space Science

Key Points:

- We analyzed marsquakes and made the first coherent detection of the SsPp phase (an SV- to P-wave reflection on the receiver side)
- We determined that the average P-wave speed in the top crustal layer (Layer 1, above 8 km) is between 2.5 and 3.2 km/s
- The average P-wave speed in Layer 1 is consistent with the current understanding of the upper crustal stratigraphy beneath InSight

Supporting Information:

Supporting Information may be found in the online version of this article.

Correspondence to:

J. Li,
jli@epss.ucla.edu

Crustal Structure Constraints From the Detection of the SsPp Phase on Mars

Jiaqi Li[1], Caroline Beghein[1], Paul Davis[1], Mark. A. Wieczorek[2], Scott M. McLennan[3], Doyeon Kim[4,5], Ved Lekić[5], Matthew Golombek[6], Martin Schimmel[7], Eleonore Stutzmann[8], Philippe Lognonné[8], and William Bruce Banerdt[6]

[1]Department of Earth, Planetary, and Space Sciences, University of California, Los Angeles, CA, USA, [2]Université Côte d'Azur, Observatoire de la Côte d'Azur, CNRS, Laboratoire Lagrange, Nice, France, [3]Department of Geosciences, Stony Brook University, Stony Brook, NY, USA, [4]Department of Earth Sciences, Institute of Geophysics, ETH Zürich, Zürich, Switzerland, [5]Department of Geology, University of Maryland, College Park, MD, USA, [6]Jet Propulsion Laboratory, California Institute of Technology, Pasadena, CA, USA, [7]Geosciences Barcelona – CSIC, Barcelona, Spain, [8]Université de Paris, Institut de physique du globe de Paris, CNRS, Paris, France

Abstract The shallowest intracrustal layer (extending to 8 ± 2 km depth) beneath the Mars InSight Lander site exhibits low seismic wave velocity, which is likely related to a combination of high porosity and other lithological factors. The SsPp phase, an SV- to P-wave reflection on the receiver side, is naturally suited for constraining the seismic structure of this top crustal layer since its prominent signal makes it observable with a single station without the need for stacking. We have analyzed six broadband and low-frequency seismic events recorded on Mars and made the first coherent detection of the SsPp phase on the red planet. The timing and amplitude of SsPp confirm the existence of the ~8 km interface in the crust and the large wave speed (or impedance) contrast across it. With our new constraints from the SsPp phase, we determined that the average P-wave speed in the top crustal layer is between 2.5 and 3.2 km/s, which is a more precise and robust estimate than the previous range of 2.0–3.5 km/s obtained by receiver function analysis. The low velocity of Layer 1 likely results from the presence of relatively low-density lithified sedimentary rocks and/or aqueously altered igneous rocks that also have a significant amount of porosity, possibly as much as 22%–30% by volume (assuming an aspect ratio of 0.1 for the pore space). These porosities and average P-wave speeds are compatible with our current understanding of the upper crustal stratigraphy beneath the InSight Lander site.

Plain Language Summary The NASA InSight mission sent a seismometer to Mars in 2018. One of the science goals of the mission is to better understand how rocky planets form and evolve by investigating the interior structure of Mars. Previous seismological studies with InSight data have revealed a shallow crustal layer (i.e., Layer 1, extending to 8 ± 2 km depth) with low seismic wave speed under the instrument. In this study, we have identified a new seismic signal on the seismograms recorded on Mars. The existence of this seismic phase confirmed the low speed of compressional (P) waves in Layer 1 and provided additional constraints on the average P-wave speed, that is, between 2.5 and 3.2 km/s. Based on these low speeds, we found that the seismic properties of Layer 1 likely result primarily from the presence of sedimentary rocks and/or aqueously altered igneous rocks that also have a significant amount of porosity, possibly as much as ~30% by volume. These porosities and average P-wave speeds are compatible with our current understanding of the upper crustal stratigraphy beneath the InSight Lander site.

1. Introduction

One of the science goals of the NASA InSight mission is to better understand how rocky planets form and evolve by investigating the interior structure of Mars (Banerdt et al., 2020). Since the landing in November 2018, the Seismic Experiment for Interior Structure (SEIS, Lognonné, et al., 2019) Very Broadband (VBB) seismometer has recorded more than one thousand events (InSight Marsquake Service, 2020, 2021a, 2021b, 2022a, 2022b). Preliminary models of the crust and mantle structure, as well as core size, have been obtained with receiver function analysis (Kim, Lekić, et al., 2021; Knapmeyer-Endrun et al., 2021; Lognonné et al., 2020), P- and S-wave differential travel-times and surface-reflected body-wave phases (Khan et al., 2021), and ScS waves (Stähler et al., 2021), respectively.

Methodology: Jiaqi Li, Caroline Beghein, Paul Davis
Project Administration: Caroline Beghein
Resources: Jiaqi Li, Paul Davis, Philippe Lognonné
Software: Jiaqi Li, Paul Davis, Doyeon Kim, Ved Lekić
Supervision: Caroline Beghein
Validation: Jiaqi Li, Paul Davis, Mark. A. Wieczorek, Doyeon Kim, Ved Lekić, Martin Schimmel, Eleonore Stutzmann, Philippe Lognonné
Visualization: Jiaqi Li
Writing – original draft: Jiaqi Li, Caroline Beghein, Mark. A. Wieczorek, Scott M. McLennan
Writing – review & editing: Jiaqi Li, Caroline Beghein, Paul Davis, Mark. A. Wieczorek, Scott M. McLennan, Doyeon Kim, Ved Lekić, Matthew Golombek, Martin Schimmel, Eleonore Stutzmann, Philippe Lognonné, William Bruce Banerdt

Using P-to-s receiver functions, Knapmeyer-Endrun et al. (2021) found two possible sets of crustal models at the lander site: a 2-layer model with a crustal thickness of 20 ± 5 km and a 3-layer model with a thickness of 39 ± 8 km depth (with a weaker impedance contrast across it). Kim, Lekić, et al. (2021) subsequently found that both S-to-p receiver functions and receiver functions constructed from free-surface P-wave multiples (PPs) favor the 3-layer model. Durán et al. (2022) also supported the 3-layer model using a more complete marsquake catalog and phase picks, though with slightly different average interface depths of 10 km, 20 km, and 45 km. Using ambient noise auto-correlation, Deng and Levander (2020), Kim, Davis, et al. (2021), and Schimmel et al. (2021) observed the strongest signal at a lag time of 10.6 s, which corresponds to a discontinuity at about 21 km depth, in agreement with the observed receiver function amplitudes.

Another prominent teleseismic signal well-recorded on Earth and often used to constrain the depth of the Mohorovičić discontinuity (hereafter referred to as Moho) is the SsPp phase, an SV- to P-wave reflection off the free surface on the receiver side. For incoming S-waves (i.e., SV-wave) polarized in the P-SV plane containing the event and the receiver, phase conversion occurs at the free surface and the converted P-waves reflect at the Moho (or any other intracrustal discontinuity) before being recorded by the seismometer (Figure 1b). On Earth, this SsPp phase has been analyzed in data from isolated stations (e.g., Owens & Zandt, 1997; Zandt & Randall, 1985; Zhou et al., 2000) and seismic arrays (Chen & Jiang, 2020; Tseng et al., 2009; Yu et al., 2012) to constrain crustal thickness. Cunningham and Lekic (2019) and Liu et al. (2019) additionally showed that SsPp phases provide complementary constraints that remove the trade-off between velocity and thickness inherent in receiver function analysis. Because there is a near-critical (sometimes post-critical) reflection within the top layer, the SsPp phase is usually stronger than an SV- to p-wave transmission in the conventional S-wave receiver function (Chen & Chen, 2020), and has been observed in several regions on Earth. For example, SsPp phases arrive at 4–11 s after the direct SV-phase in the western United States (Yu et al., 2016), 7–12 s across the North China craton (Yu et al., 2012), and 12–18 s across the Himalayan-Tibetan orogeny (Tseng et al., 2009).

In continental regions on Earth, the Moho lies between depths of about 15 and 75 km (e.g., Brown & Mussett, 1993; Chen et al., 2013; Laske et al., 2013). When there are no sedimentary basins, the Moho is usually where the most significant jump in seismic wave speed occurs within the lithosphere of the average Earth model (e.g., Kennett & Engdahl, 1991). At the Mars InSight lander site, the situation is different, and the interface with the largest wave speed change corresponds to the shallowest intracrustal layer, hereafter referred to as Layer 1, at 8 ± 2 km (Knapmeyer-Endrun et al., 2021). The velocity contrast is estimated to be up to +40% due to the relatively low wave speed within Layer 1.

The low velocity and recently discovered seismic anisotropy of Layer 1 (Li et al., 2022), make it an important region to study since both features are likely related to high porosity in the Martian crust (Knapmeyer-Endrun et al., 2021; Li et al., 2022). The low observed velocities could potentially be a result of sedimentary or volcanic ash and pyroclastic deposits that have intrinsically high porosity, or a high density of fractures in the upper crust generated by impact cratering events, such as is observed on the Moon (e.g., Milbury et al., 2015; Soderblom et al., 2015; Wieczorek et al., 2013). Alternatively, the low velocities could be the result of a high quantity of aqueously altered materials (Lognonné et al., 2022). Understanding the origin of the low seismic velocity in this layer would not only provide clues to the origin of this layer but would also provide useful information for future studies of the deeper crustal layers (e.g., Wieczorek et al., 2022).

The large amplitude characteristics of SsPp and the previously observed large wave speed jump across the base of Layer 1 make the SsPp an ideal phase to further constrain the properties of Layer 1. In addition, because it can be observed with a single station without the need for stacking, this phase is naturally suitable for seismic studies on Mars where we only have one instrument at a single location on the planet.

2. Data and Methods

There are two main criteria for SsPp data selection on Earth. First, the epicentral distance should be larger than 30° to avoid mantle triplications generated by the 410-km and 660-km discontinuities (Kang et al., 2016). On Mars, the ideal epicentral distance to detect SsPp should be smaller than 60°, since the phase transformation of olivine to its higher-pressure polymorphs occurs at around 1,000 km depth (Huang et al., 2022).

Second, the source wavelet should be simple. Deep earthquakes are therefore usually preferred (e.g., Tseng et al., 2009) since their source time function is often simple, and the depth phases from deep earthquakes, which
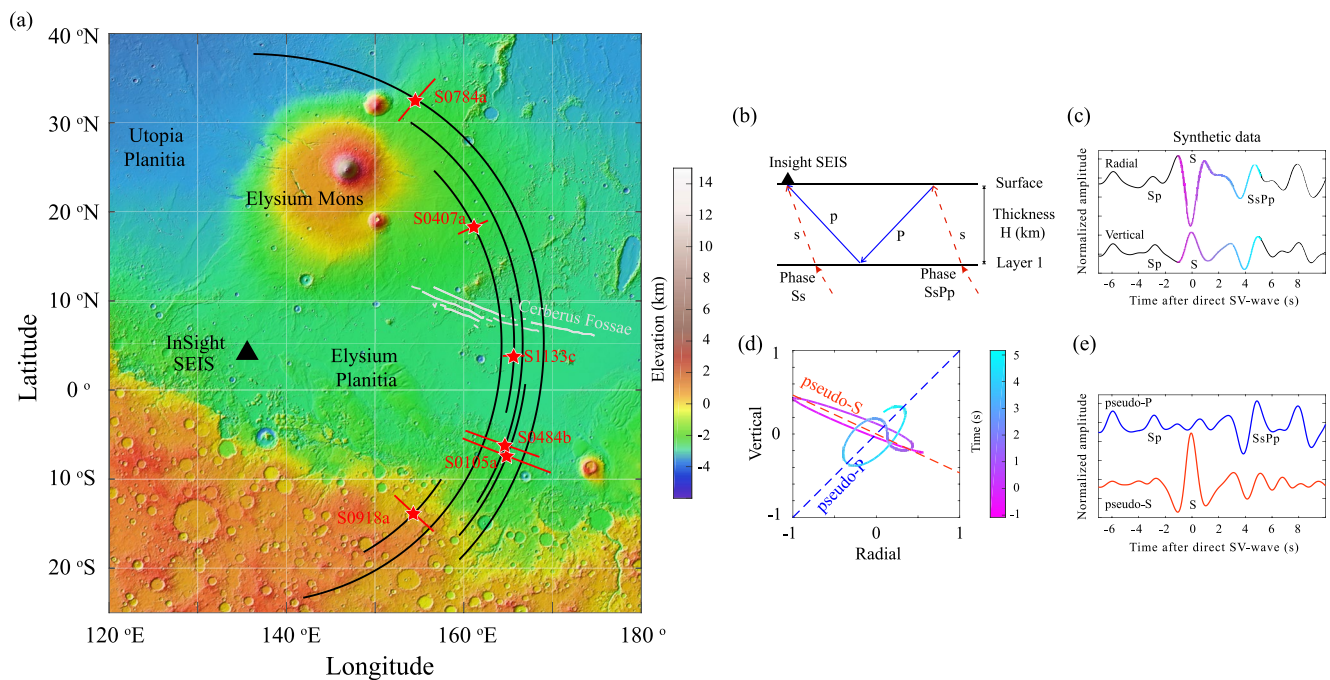
Figure 1. (a) Topographic map from the Mars Orbiter Laser Altimeter (MOLA, Smith et al., 2001) near Seismic Experiment for Interior Structure (SEIS) (black triangle). The red stars mark the six events used in this study. The red and black error bars indicate the uncertainties in epicentral distance and back azimuth, respectively (see Supporting Information S1, Section 1.1). (b) Ray paths of the SsPp phase from a planar, incident teleseismic SV-wave near the SEIS instrument. The S-waves are shown as dashed red lines and the converted P-waves are in blue. (c) Synthetic waveforms on the radial and vertical components. Colorscales correspond to the arrival time of the traces. (d) Particle motion analysis for part of the waveforms (−1 to 5 s) on the radial and vertical components shown in (c). Colorscales correspond to the arrival time of the traces, and are the same as in (c). Oblique lines indicate the estimated direction for the pseudo-P (in blue) and pseudo-S (in red) components. (e) Synthetic waveforms on the pseudo-P (in blue) and pseudo-S (in red) components, derived from the particle motion analysis in (d).

arrive later, do not interfere with SsPp. This criterion could have been a problem to detect SsPp on Mars since most of the events detected so far likely originate from depths shallower than 40 km (Drilleau et al., 2021; Durán et al., 2022). Nevertheless, Yu et al. (2013) showed that this problem could be mitigated by removing the source wavelet complexity resulting from source-side scattering. Specifically, analyses of particle motion provide clues for deriving a "pseudo-S" wave train, which contains information about both the source time function and depth phases. After the deconvolution of this "pseudo-S" wave train, the authors showed that shallow events with complex source wavelets display signals in the seismic data of similar clarity to those from deep earthquakes (Yu et al., 2013). This method thus greatly increases the number of earthquakes that can be used to study SsPp phases and makes it possible to look for them on Mars.

In addition to these two criteria, we found that the duration of the source wavelet, which is measured based on the direct SV phase (Ss), plays a crucial role in reliably detecting SsPp phases on Mars, and that it needs to be relatively short. On Earth, the SsPp phase is mostly used to study the Moho and arrives at relatively large differential travel times to the Ss phase (e.g., 4—11 s in the western United States (Yu et al., 2016)). This implies that even a relatively long source wavelet duration does not affect the SsPp detection. On Mars, however, the base of Layer 1 is located at about 8 km depth and synthetic waveforms (where the source time function has a short duration of 1 s) predict differential arrival times of only about 4 s (Figure 1c). This means that if the source time function has a relatively long duration, the SsPp phase will likely be buried in the Ss phase source wavelet, making it undetectable directly (Figure S1 in the Supporting Information S1). We verified that as long as the duration of the source wavelet is less than $T_{SsPp} − T_{Ss}$, the particle motions show linear trends and the source-normalization technique (Yu et al., 2013) can effectively obtain the corresponding SV- to P-phase (e.g., Figure S1f in the Supporting Information S1). On the contrary, if the duration of the source wavelet is larger than $T_{SsPp} − T_{Ss}$, the particle motions no longer exhibit linear trends (Figures S1d and S1e in the Supporting Information S1), and the short time function approximation cannot be applied, in which case the derived SsPp phase is unreliable (Figure S1c in the Supporting Information S1).

Locating marsquakes using a single station is challenging because both the arrival times of P- and S-waves and P-wave polarization information are needed to determine the epicentral distance and the back azimuth, respectively. During 1,133 Mars solar days (i.e., over three Earth years), SEIS has recorded 32 broadband (with energy up to 2.4 Hz) and 52 low-frequency (with energy below 1 Hz) marsquakes, and only 11 of them are labeled "quality-A" by the InSight Marsquake Service (MQS) 2020, 2021a, 2021b, 2022a, 2022b. To be designated quality A, an event needs to have both clear back azimuth and epicentral distance. Quality-A marsquakes, in most cases, are ideal candidates for many seismological studies due to their strong seismic energy, high signal-to-noise ratio, and well-constrained event location. However, most of the quality-A events happen to have relatively long source wavelets (Figure S2 in the Supporting Information S1), therefore, are not necessarily ideal for analyzing SsPp phases.

To date, nine quality-A events have an epicentral distance smaller than 60° (Figure S2 in the Supporting Information S1). Four of them (S0235b, S1015f, S1022a, and S1048d) exhibit very long (e.g., larger than 5 s) and complex source wavelets, indicating that they are not suitable for our SsPp study. There is less low-frequency content in the source time function of the other five quality-A events (S0173a, S0809a, S0820a, S0864a, and S1133c) and although multiple peaks or oscillations are observed, they are potential candidates for this study.

Compared with quality-A events, marsquakes of quality B, in general, have shorter and simpler source wavelets. There are 18 marsquakes of quality B (eight broadband and 10 low-frequency), and the epicentral distances have been measured to be within 60° (with an uncertainty smaller than 10°) for 12 of them. However, due to their relatively low signal-to-noise ratio, the MQS has not determined the back azimuth for the quality-B events. Recent studies by Drilleau et al. (2021) and Zenhäusern et al. (2022) with detailed analyses of the waveforms provided back azimuth estimates for 10 of these 12 events. After excluding event S0325a whose estimated back azimuth shows large discrepancies between the two studies, we are left with a total of nine quality-B events with both epicentral distance and back azimuth information.

In this study, we focused on seven of these nine quality-B events with back azimuths between 0 and 180° (Table S1 in the Supporting Information S1) and which are in the same direction (to the east of the InSight lander) as the events used in the receiver function study (Knapmeyer-Endrun et al., 2021). Besides these seven quality-B events, we also included one quality-A event S1133c, which has a relatively short source time function of ~4 s. Comparisons with the other eight quality-A events can be found in the Supplementary Material (i.e., Figures S2 and S3 in the Supporting Information S1).

2.1. Data Processing

The waveform data (InSight Mars SEIS data service, 2019) were processed by first applying a pre-filtering from 0.01 to 8 Hz (zero-phase, second-order Butterworth filter) to the deglitched data set (Scholz et al., 2020, with a sampling rate of 20 samples per second), and then removing the instrument response to get the ground motion records. Finally, we filtered (zero-phase, second-order Butterworth filter) the data into periods from 1.5 to 5 s. We prefer working with the displacement record because there are fewer oscillations compared with the velocity record.

To analyze the SsPp, we need to use data from the radial (R) and vertical (Z) components. We thus converted the waveforms from the original UVW to NEZ channels using ObsPy (Beyreuther et al., 2010) and rotated the coordinates from NEZ to RTZ using the back azimuth information provided by previous studies (Drilleau et al., 2021; Zenhausern et al., 2022) and listed in Table S1 in the Supporting Information S1.

2.2. SsPp Phase

Figure 1b illustrates the ray path of the SsPp phase, where the Ss-leg of the ray path (the dashed line in red to the right of the lander) is almost parallel to that of the direct SV phase (the dashed line in red below the lander). The major difference between the ray paths is the near- or post-critical Pp reflection at the base of Layer 1. Therefore, the travel-time difference between the direct Ss phase and SsPp phase can provide constraints on the average P-wave speed and thickness of Layer 1:

$$T_{SsPp-Ss} = 2H\eta_\beta = 2H\sqrt{\frac{1}{V_P^2} - p_\beta^2}, \tag{1}$$
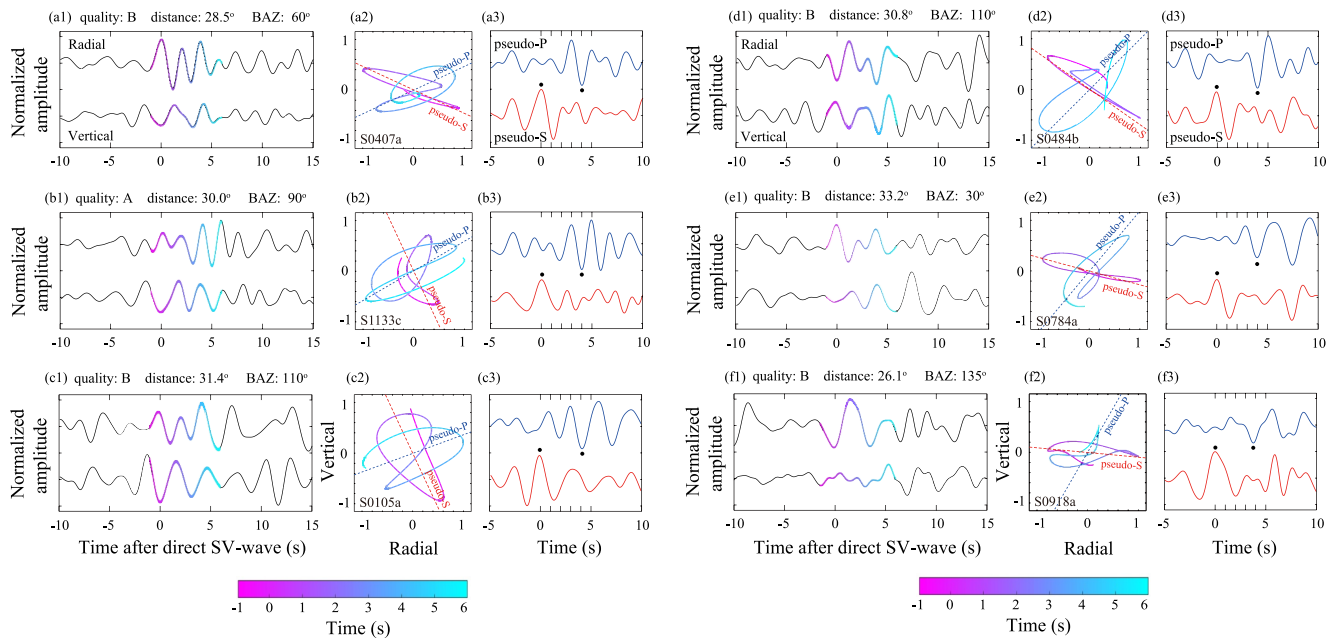
Figure 2. (a1) Raw displacement waveforms on the radial and vertical components for event S0407a. The layout is the same as Figure 1c. (a2) Particle motion analysis for event S0407a. The layout is the same as Figure 1d. (a3) Separated waveforms on the pseudo-P and pseudo-S components for event S0407a. The peak on the pseudo-S component (at around 0 s) and the trough on the pseudo-P component (at around 4 s) are indicated by black dots. Same analysis for event S1133c (b1-b3), S0105a (c1–c3), S0484b (d1–d3), S0784a (e1–e3), and S0918a (f1–f3). Note that the waveforms are flipped if needed to make the amplitude at 0 s on the pseudo-S component to be positive for better illustration.

where η_β and p_β are the vertical and horizontal slowness (i.e., ray parameter) of the incident SV wave, respectively. V_P is the average P-wave speed in the layer, and H is its overall thickness.

We first calculated synthetic seismograms for the radial (*R*) and vertical (*Z*) components using a MATLAB package (Yu et al., 2017) based on the propagator method (Kennett, 2009) with a planar incident SV-wave (with a delta source wavelet, filtered between 1.5 and 5 s). Using one of the models from the receiver function study (Knapmeyer-Endrun et al., 2021) with a Layer 1 thickness of 8 km and an average P-wave velocity of 3.0 km/s, we found that the simulated SsPp phase arrives about 4 s after the direct SV phase for marsquakes with an epicentral distance of 30° (i.e., a ray parameter of 13.3 s/deg). This SsPp phase is observable on both the radial and vertical components (Figure 1c).

Particle motion analysis of the radial and vertical components of the synthetics shows that the first signal (at −1 to 2 s) and the second signal (at 3–5 s) have distinctive particle motions. Specifically, the first signal follows a linear trend in the second and fourth quadrants, and the second signal is polarized in the first and third quadrants (Figure 1d). We can define pseudo-S and pseudo-P components according to the direction of these two sub-linear particle motions (Yu et al., 2013). On the pseudo-S component, the main phase is the direct SV phase at 0 s (Figure 1e). On the pseudo-P component, there is no direct SV phase at 0 s, but a strong SsPp phase is visible at around 4 s (Figure 1e).

We applied the same particle motion analysis and the pseudo-P and S separation technique to the real data. Figure 2 shows examples of quality-A event S1133c, quality-B events S0105a, S0407a, S0484b, S0784a, and S0918a. In Figure 2, the start time (0 s) is selected based on the arrival time of the S-wave measured by MQS (Table S2 in the Supporting Information S1), where the signal envelope is analyzed in multiple narrowband filters and the coherent start time in the largest possible bandwidth is selected (Clinton et al., 2021). In all cases, there are two linear trends in the particle motion analysis and there is a strong signal at around 4 s on the pseudo-P components. The following analysis is based on these six events, and we excluded the other two quality-B events due to no clear pseudo-P and S separation (S0409d, in Figure S4a in the Supporting Information S1), and no clear direct-SV arrival (S0802a, in Figure S4b in the Supporting Information S1).
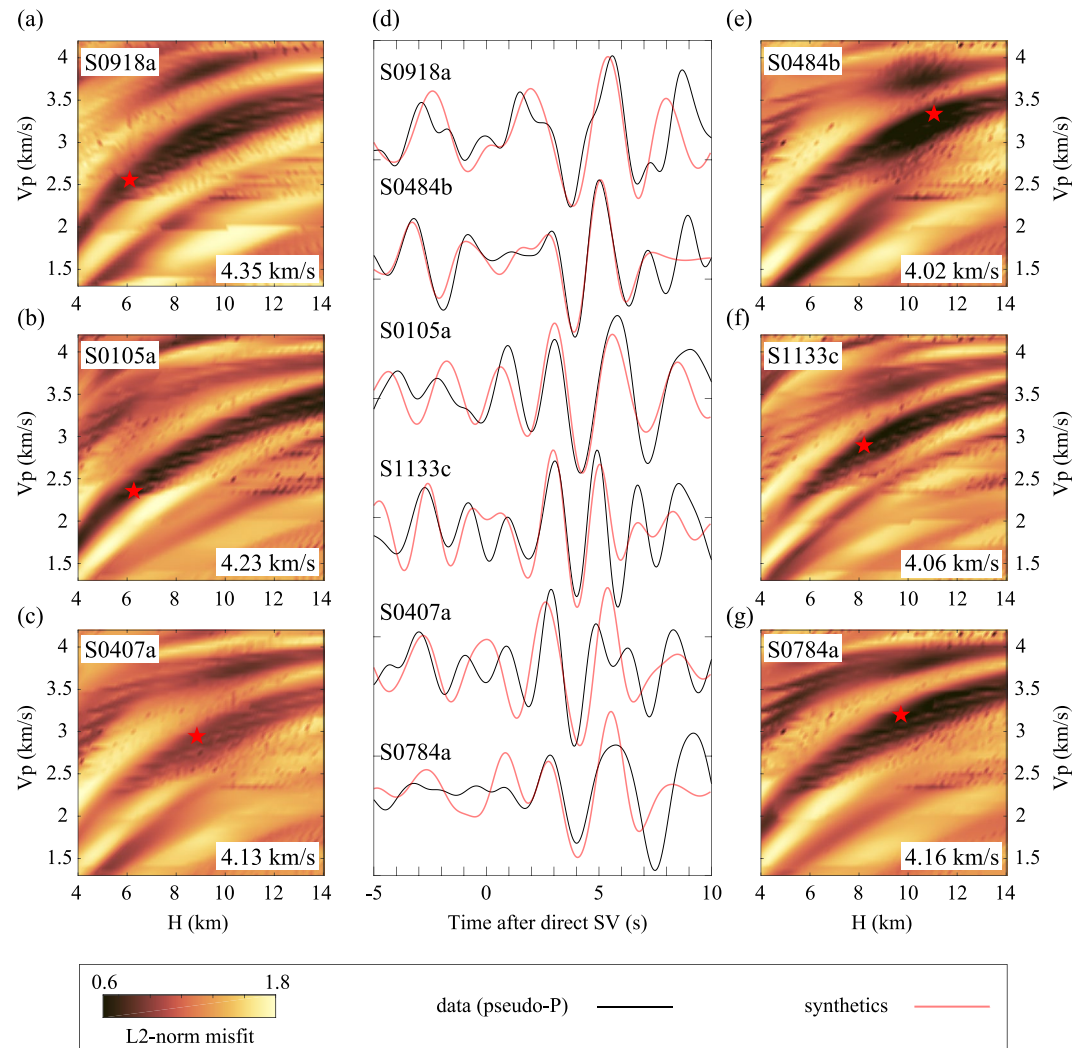
Figure 3. (a) L2-norm misfit map for event S0918a. The red star marks one of the acceptable models within the strict threshold of Figure 4b, and the P-wave speed of the second layer is shown in the lower right corner. The corresponding synthetic waveforms are shown in (d) in the same color. (b) L2-norm misfit map for event S0105a. (c) L2-norm misfit map for event S0407a. (d) Comparison between data (in black) and synthetics (in red) on the pseudo-P components. (e) L2-norm misfit map for event S0484b. (f) L2-norm misfit map for event S1133c. (g) L2-norm misfit map for event S0784a.

Although the arrival times of the signals on the pseudo-P components are coherent, their waveforms vary between different events. This is mainly due to the different source time functions, which are indicated by the phase at 0 s on the pseudo-S components. To consider the effect of different kinds of source wavelets, we followed Yu et al. (2013) to assume the waveforms on the pseudo-S component to be an approximation of the source wavelet and then convolved the assumed source wavelet (from −5.0 s to +2.5 s) with the synthetic Green's function to simulate the pseudo-P component (Figure 3).

3. Results

3.1. Waveform Comparison and Misfit Map

In the SsPp phase, there is a near- or post-critical Pp reflection at the base of Layer 1, and thus a phase shift might occur. When such a phase shift happens, it prevents us from accurately picking the arrival time of SsPp (e.g., Figure S6 in the Supporting Information S1). Therefore, we prefer to perform a waveform comparison (between the data and the synthetics) rather than refer to Equation 1, to constrain the model parameters (i.e., the average P-wave speed and thickness of Layer 1).

(a)   (b)
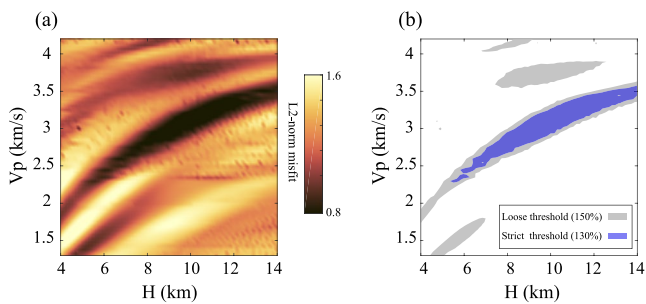
Figure 4. (a) Summed L2-norm misfit map for the SsPp data. (b) Acceptable model regions defined by the loose (in gray) and strict (in blue) thresholds extracted from (a).

To compare the synthetic SsPp waveforms with the real data, we first applied the same particle motion analysis to the synthetic vertical and radial Green's functions to separate the synthetic pseudo-P and pseudo-S components, then we convolved the synthetic pseudo-P waveforms with the source wavelet (derived from the real data) to simulate the observations. We found that the simulated waveforms (i.e., the red waveforms in Figure 3d), generated by the acceptable models (i.e., corresponding to the red stars in Figure 3), match the pulse at around 4 s in the data well.

Although these models predict waveforms that are similar to the data, trade-offs between model parameters (the average P-wave speed and layer thickness) exist as shown in Equation 1. To find all acceptable models, we performed forward modeling and sampled the average P-wave speed (from 1.3 km/s to 4.2 km/s with an interval of 0.02 km/s) and layer thickness (from 4 to 14 km with an interval of 0.05 km) of Layer 1. Since the velocity of the second layer will affect both the amplitude and the phase of the SsPp signal (Figure S6 in the Supporting Information S1), we also varied the velocity of the second layer (from 1.1 to 1.8 times the velocity of Layer 1 in 0.1 intervals). Of these three parameters, the Layer 1 thickness and average P-wave speed are more directly related to the differential arrival time (e.g., Equation 1), and the velocity of the second layer affects the possible phase shift of the SsPp (i.e., the waveform of SsPp, also see Figure S6 in the Supporting Information S1). Therefore, although we simultaneously searched for three parameters to better fit the waveforms, we only aimed to constrain the thickness and average P-wave speed of Layer 1, whereas the velocity of the second layer is more difficult to constrain given the relatively low signal-to-noise ratio on Mars compared with that on Earth (e.g., Liu et al., 2019).

At each grid cell, we calculated synthetic Green's functions, performed the particle motion analysis, separated the synthetic pseudo-P and pseudo-S components, convolved the assumed source wavelet (i.e., S wave, from −5.0 s to +2.5 s, on the pseudo-S or the tangential component), and then compared the simulated waveforms with the data. To quantify the waveform similarity between the data and the synthetics, we selected a misfit window from −5.0 to 6.0 s. We chose the L2-norm of the waveform differences (after normalization) in the time domain as the misfit function. The misfit maps are shown in Figure 3. Models in the dark regions have smaller misfits and are thus more acceptable than models in the bright area. We found that the average L2-norm misfit along the approximate diagonal (i.e., regions close to the predictions from the ray theory with Equation 1) is systematically lower, confirming our identification of the SsPp phase.

We note that there is another signal at around −2.5 s in the data which is also fitted by the synthetics. This phase is likely to be the S-to-p transmission at the base of Layer 1 (i.e., the S-to-p receiver function), and could provide additional constraints on the properties of Layer 1 (e.g., Chen & Chen, 2020). However, due to its relatively smaller amplitude compared with the SsPp, this phase has a limited contribution to the total misfit.

To suppress the data noise, we averaged the L2-norm misfit maps (with the same weight) to get the final misfit map in Figure 4a. We first found the best-fitting model with the smallest misfit, then defined the range of acceptable models using a misfit threshold (i.e., strict and loose thresholds were set for misfits within 130% and 150% of the minimum misfit, respectively). Those strict and loose thresholds were set to extract the acceptable region of the model space (i.e., Figure 4b). We also see that there are other sets of solutions (e.g., near the lower left corner and near the top in Figure 4b) in addition to the one along the approximate diagonal. Nevertheless, those solutions are of relatively larger misfits and are only observed with the loose misfit threshold.

Although the choice of the L2-misfit threshold is somewhat subjective, we are confident our analysis is robust because we tested several thresholds and compared them with predictions from ray theory. For example, if we consider an even smaller threshold value of 110% of the minimum misfit, there are very few acceptable regions, indicating that this threshold is too strict to be used in practice (in Figure S7a in the Supporting Information S1). We also compared the acceptable regions (derived from the L2-norm misfit maps) with the ray-theory-based calculation using formula 1. The first-order trends are similar between these two approaches (Figure S7 in the Supporting Information S1). In addition, the choice of the misfit function (e.g., L2-norm, L1-norm, or cross-correlation coefficient) does not affect the pattern of the misfit map (Figure S8 in the Supporting Information S1).
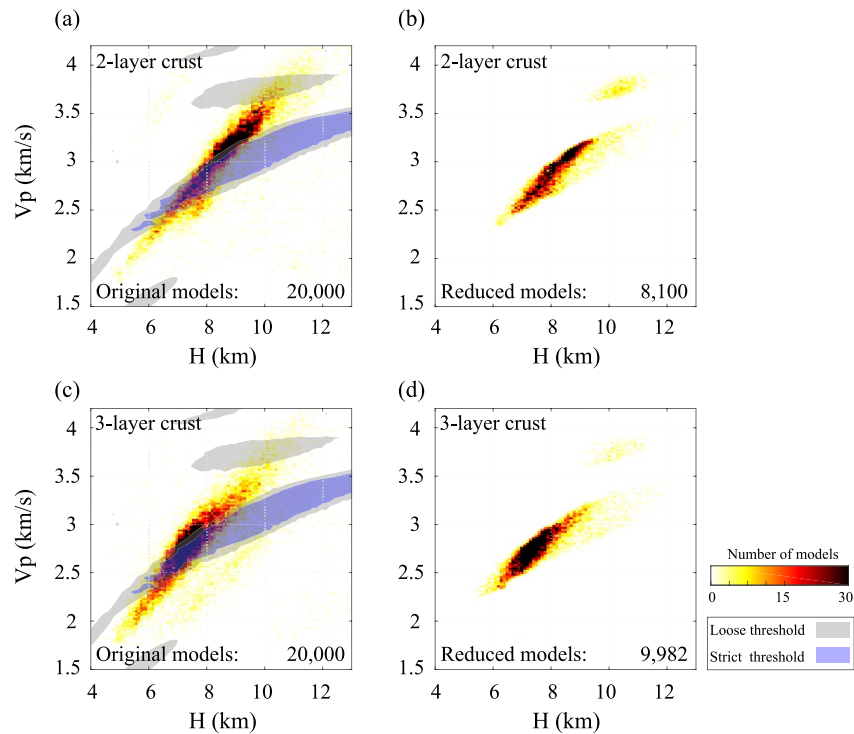
Figure 5. (a) Colored dots represent the original 20,000 models from the receiver function study (Knapmeyer-Endrun et al., 2021) for the 2-layer crustal case. The color scale indicates the number of models at each grid point. The acceptable model regions with the loose (in gray) and strict (in blue) thresholds derived from the SsPp data in this study are superimposed. (b) Reduced models for the 2-layer crustal case with the constraint from the SsPp phase in this study. (c) Same as (a) for the 3-layer crustal case. (d) Same as (b) for the 3-layer crustal case.

We note, however, that there are discrepancies between our derived acceptable regions and the ray-theory-based predictions (Figure S7 in the Supporting Information S1). These arise because, when the velocity of the second layer is large enough, the SsPp is a post-critical reflection and a phase shift occurs. In such a case, the location of the negative pulse deviates from the actual arrival time of the SsPp phase (Figure S6 in the Supporting Information S1). Therefore we trust the results from the misfit map since the possible phase shift (for the critical P-p reflection off Layer 1) is included in the synthetics calculations. In addition, multiple sources of uncertainties are automatically included in the final misfit map such as the noise in the data, the duration of the pulse, and even finite-frequency effects.

3.2. Constraints From SsPp

Our study provides constraints on the average P-wave velocity in Layer 1 using the SsPp phase, which can be compared to the acceptable models in the receiver function study (Knapmeyer-Endrun et al., 2021). In Figures 5a and 5c, we first plotted the distribution of the average P-wave speed and thickness of Layer 1 from the receiver function study (Knapmeyer-Endrun et al., 2021), for the 2-layer and 3-layer crust cases, respectively. In each case, there are 20,000 acceptable models, and most of those models are located along a sub-linear trend reflecting the trade-offs between the wave speed and layer thickness.

Then, we superimposed the acceptable model space regions determined from our SsPp analysis for the strict and loose thresholds (blue and gray regions, respectively). For both the 2-layer (Figure 5a) and 3-layer (Figure 5c) cases, acceptable regions derived from the SsPp analyses intersect with the models from Knapmeyer-Endrun et al. (2021). Because the acceptable ensemble of models derived from the SsPp analysis has a different slope compared to the models obtained with receiver functions, the trade-offs between model parameters and the number of possible models can be reduced. That is, models located at the intersection of the two regions are accepted by both the receiver function and the SsPp data. When they are outside the loose threshold contours,
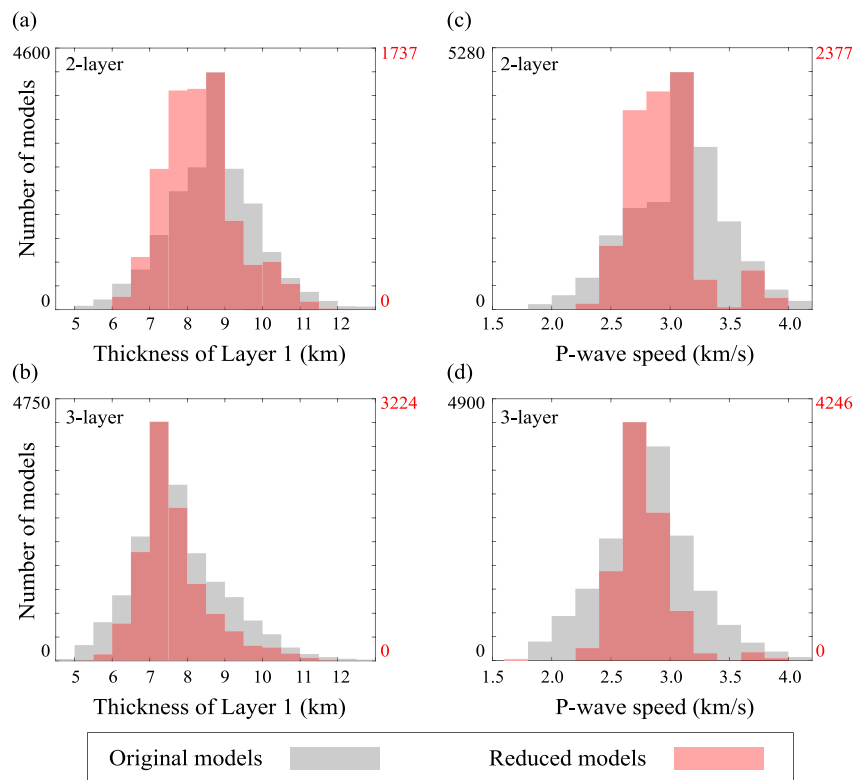
Figure 6. (a) Histograms for the thickness of Layer 1 in the original 2-layer crustal case (in gray) of Knapmeyer-Endrun et al. (2021) and reduced model ensemble (in red). (b) Histograms of the average P-wave speed in Layer 1 for the 2-layer crustal case. (c) Same as (a) for the 3-layer crustal case. (d) Same as (b) for the 3-layer crustal case.

those models are rejected. Models lying in between the two thresholds have a certain chance of being accepted, according to their misfit (e.g., smaller misfits correspond to larger acceptance possibilities).

With this new constraint, the total number of possible models is reduced from 20,000 to 8,100 for the 2-layer crustal case, and from 20,000 to 9,982 for the 3-layer crustal case (Figures 5b and 5d). The most prominent feature of these smaller model sets is a cut-off P-wave speed of about 3.2 km/s.

3.3. Average P-Wave Speed and Thickness of Layer 1

In Knapmeyer-Endrun et al. (2021), two ensembles of crustal models were shown to be compatible with the receiver function data: a 2-layer model and a 3-layer model. However, discrepancies were found between the two sets of models, for both the average P-wave speed and the thickness of Layer 1 (i.e., gray histograms in Figure 6): the preferred thickness for Layer 1 is 8.5–9.0 km for the 2-layer case and 7.0–7.5 km for the 3-layer case, and the preferred average P-wave speed for Layer 1 is 3.0–3.5 km/s for the 2-layer case and 2.5–3.0 km/s for the 3-layer case. These discrepancies might be because the properties of Layer 1 (e.g., velocity and thickness) have to be able to explain both the Ps phase and its multiple PpPs phase for the 2-layer crustal case (Knapmeyer-Endrun et al., 2021).

The analyses we performed in the present work allow us to obtain new distributions (i.e., red histograms in Figure 6) of possible average P-wave speed and thickness for Layer 1 (Cunningham & Lekic, 2019; Liu et al., 2019) in both the 2-layer case and the 3-layer case. Using the ensemble of models obtained with our additional constraints from the SsPp data, we found that the preferred thickness of Layer 1 for the 3-layer crust case remains unchanged (7.0–7.5 km). However, the preferred thickness for the 2-layer crust case is shallower (7.5–9.0 km) than in the original receiver function study (8.5–9.0 km, from Knapmeyer-Endrun et al., 2021). The preferred average P-wave speeds in both cases are centered between 2.5—3.2 km/s, which is also seen in Figure 5. In addition, the estimated average P-wave speed and thickness of Layer 1 are more consistent between

the two cases when adding our SsPp constraints to the original receiver function study. However, based solely on our SsPp analysis and the receiver function analysis of Knapmeyer-Endrun et al. (2021), we cannot distinguish between a 2-layer and a 3-layer crust.

4. Discussion

4.1. Method Validation

The separation of the pseudo-SV and pseudo-P wave trains is key to removing the source-side scatterings and enhancing the signals from the structure. In this study, we estimated those based on a particle motion analysis (Yu et al., 2012). This approach is fully based on the data and does not rely on a priori knowledge of the near-surface. However, the results could be affected by the presence of noise. To test the influence of the possible noise, we also applied a free-surface transform matrix (Kennett, 1991), constructed from prior information about the P- and S-wave speeds of the near-surface from Kim, Lekić, et al. (2021), to estimate the P- and SV-waveforms. Results show that the derived pseudo-S and pseudo-P wave trains from this free-surface transformation are consistent with those from the particle motion analysis (see Supporting Information S1, Section 1.2).

To search for acceptable models, we performed grid searches for three parameters: the average P-wave velocity and the thickness of Layer 1, and the P-wave velocity of the second layer. An alternative way to assess our results is to directly use the 40,000 receiver-function-derived models (Knapmeyer-Endrun et al., 2021) to calculate the synthetic SsPp waveforms and compare them with the SsPp data. Results show that both approaches exhibit the same first-order pattern: models with an average P-wave velocity larger than 3.2 km/s are rejected. This implies that the upper limit of the average P-wave velocity (at around 3.2 km/s) is required by the data and is not dependent on the inversion approach (see Supporting Information S1, Section 1.3).

We further analyzed the model uncertainties resulting from location error (i.e., epicentral distance and back azimuth) and glitches (see Supporting Information S1, Section 1.1). We also investigated the possible interferences with other signals (see Supporting Information S1, Section 1.4), the sharpness and dip of the interface (see Supporting Information S1, Section 1.5), the effects of different data types (i.e., displacement or velocity records, see Supporting Information S1, Section 1.6), and compared our models with auto-correlation results (see Supporting Information S1, Section 1.7). We concluded that our derived average P-wave speed in Layer 1 (between 2.5 and 3.2 km/s) is robust.

4.2. Origin of Layer 1

The low average P-wave speed in Layer 1 indicates the presence of materials with low seismic velocity in the upper crust at the InSight landing site. Low seismic velocities, in turn, imply materials with low density (compared to the middle or lower crust), that could result from elevated porosity (e.g., Lognonné et al., 2020), low-density lithologies (including chemically altered lithologies), or a combination of intrinsically low-velocity materials and porosity (e.g., Wieczorek et al., 2022).

The near-surface geology and stratigraphy in the vicinity of the InSight landing site are now reasonably well understood although the constitution of the deeper crust (i.e., >0.2 km) is less well constrained (Golombek et al., 2020; Pan et al., 2017, 2020; Warner et al., 2022). The subsurface at the InSight landing site includes a shallow impact-generated regolith (several meters thick) that grades into ~170 m of Early Amazonian to Hesperian basalt lava flows that are underlain by sedimentary rocks of the Noachian age (Golombek et al., 2017, 2018; Pan et al., 2020; Warner et al., 2022). Orbital imaging and spectral evidence from lithologies thought to be excavated in nearby craters suggest that rocks at greater depth are characterized by Fe/Mg-bearing phyllosilicates and are interpreted to be either Noachian sedimentary rocks (Warner et al., 2022; also see Pan et al., 2020) or aqueously altered Noachian igneous rocks (Pan et al., 2017), or presumably some combination, and that could extend to depths up to 5 km—possibly the entire thickness of Layer 1.

4.2.1. Porosity Effects

Since all of the possible Layer 1 lithologies (sedimentary, volcanic, altered Noachian basement) in the vicinity of the landing site could contain significant porosity, we first consider the influence of porosity alone on seismic wave speed.
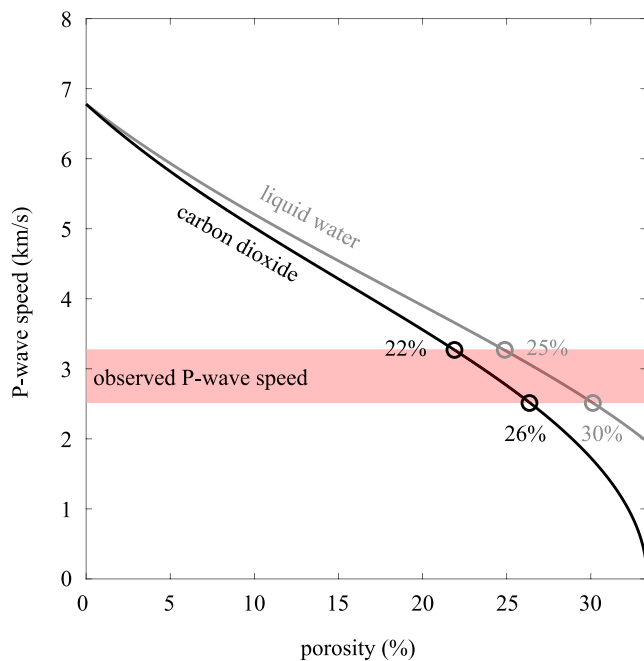
Figure 7. P-wave speed of porous basalt with intrusions of carbon dioxide (in black) and liquid water (in gray) as a function of porosity (with the aspect ratio of 0.1). The shaded red region marks the range of the average P-wave speeds from this study. The derived lower and upper limits for the porosity estimations are also indicated.

Here, we assess how porosity affects the wave speed of typical Martian basaltic materials. This will provide us with a maximum allowable porosity, given that other materials (e.g., sedimentary rocks) have intrinsically lower wave speeds.

We make use of the scattering theory of Toksöz et al. (1976) to estimate the P-wave speeds of a given material as a function of porosity. As demonstrated by Heap (2019), the bulk seismic velocity depends upon the matrix composition, the amount of porosity, the composition of the material filling the pores, and the pore aspect ratio. We have performed similar calculations as in that study and compared the predicted wave speeds with our average P-wave speed results for Layer 1 beneath the InSight lander. For the model setup, we assumed a basaltic composition for the matrix, given that basalts are the dominant rock type found near the surface of Mars (e.g., McSween et al., 2009). Such a composition could be representative of either basaltic lavas or the detrital grains of unaltered basaltic sediment (e.g., McLennan et al., 2019). After including a specified porosity, the pore space was filled with either atmospheric gas (e.g., carbon dioxide) or liquid water. Manga and Wright (2021) demonstrated that the observed low S-wave speeds in the upper 8 km beneath the InSight lander preclude the existence of water ice in this layer, so we did not consider this case further in our analysis.

We plotted our predicted P-wave speeds in Figure 7. A seismic velocity of 6.8 km/s was assumed for non-porous basaltic materials (Christensen, 1972), a pore aspect ratio of 0.1 was assumed (Heap, 2019), and properties of the void filling materials were also taken from Heap (2019). We see that as the porosity increases, the P-wave speed in the layer decreases, being reduced by a factor of two for porosities close to 20%–25%. The P-wave velocity is somewhat larger when the pores are filled by liquid water than by atmospheric gas, but the difference is only moderate for the majority of the range of porosities that we consider. Our average P-wave speeds for the upper 8 km of Mars from InSight data (from 2.5 to 3.3 km/s) can be accounted for by a porosity of 25%–30% when the pores are filled by liquid water, or 22%–26% when the pores are filled by atmospheric gas. If the pores were more spherical than our assumed aspect ratio of 0.1, the amount of required porosity would be greater (see Heap, 2019). In contrast, if the seismic velocity of the matrix materials was lower than assumed, the amount of required porosity would be reduced.

Our computed porosities are consistent with the range of values found for a variety of typical extrusive rocks at volcanoes on Earth, which can approach 30% (see data tabulated in Lesage et al., 2018) and for clastic sediments that often exceed 30% (e.g., Boggs, 2009). On the other hand, these porosities are somewhat higher than those directly measured in Martian meteorites, with porosities mostly in the range of 2%–12% (Coulson et al., 2007).

Though near-surface volcanic deposits can form with high porosities over a range of length scales (from gas bubbles in magmas to evacuated lava tubes), impact cratering is an additional mechanism that can fracture and generate significant porosity in crustal materials. As an example, combined gravity and remote sensing data imply that the average porosity of the crust of the Moon is about 12% (Wieczorek et al., 2013) and that the porosity could be even higher for the uppermost crust (Besserer et al., 2014). Analyses of feldspathic samples from the lunar highlands reveal impact-generated porosities that range from about 2% to 20% (Kiefer et al., 2012). Drill core samples from the central peak ring of the Chixulub impact basin have similar average porosities as the lunar samples, near 12% at depths near a kilometer, with values that reach as high as 20% at shallower depths (Rae et al., 2019). Drill cores from within the Reis impact crater on Earth also show the presence of up to about 30% porosity in the upper few hundred meters (Förstner, 1967). Given the ancient age of the surface volcanic materials at the Insight landing site (from Hesperian to Early Amazonian, see Warner et al., 2022), combined with the presence of an about 10 m thick impact generated regolith at the surface in the vicinity of the landing site, impact processes could have plausibly contributed to high levels of porosity in the upper 8 km of the crust beneath the InSight lander.

4.2.2. Lithological Effects

When considering lithological effects, it is also convenient to think in terms of rock density since seismic velocities for several different possible lithologies are more difficult to directly predict in any systematic manner. Although it is well known that there is a relationship between seismic velocities and rock density, the detailed nature of that relationship is less certain (e.g., Brocher, 2005). Nevertheless, values of the average P-wave speeds in the range of 2.5–3.3 km/s likely correspond to rock densities in the range of about 2,000 to 2,300 kg m^{-3} (Brocher, 2005; Christensen & Salisbury, 1975; Gardner et al., 1974), compared with an average crustal grain density of <3,100 kg m^{-3} (Wieczorek et al., 2022; also see Taylor & McLennan, 2009).

In Figure 7, we assumed that porosity-free upper crustal basaltic rocks have a P-wave speed of 6.8 km/s which is broadly consistent with the average crustal bulk density that is constrained to be <3,100 kg m^{-3} (Wieczorek et al., 2022). However, recent findings from rover activities in Gale crater and lithologies preserved in the Martian meteorite breccia NWA7533 (and its numerous pairs) indicate that the early crust of Mars is lithologically diverse (e.g., Cousin et al., 2017; Humayun et al., 2013) with compositions ranging from picrobasalt ($SiO_2 < 45\%$) through to alkali-rich intermediate-felsic compositions ($SiO_2 > 60\%$). Wieczorek et al. (2022) estimated the grain densities for known igneous lithologies and found them to be in the range of 2,680–3,420 kg m^{-3}, thus varying by over 25% relatively. Accordingly, there is a possibility that at least some of the igneous materials making up the upper crust in the vicinity of InSight have porosity-free P-wave velocities that are lower than the 6.8 km/s assumed here.

The favored interpretation of the presence of several kilometers of Noachian sedimentary rocks beneath the landing site is consistent with our current understanding of the scale of the Martian sedimentary record. Based on geochemical mass balance, McLennan (2012) estimated the minimum size of the Martian sedimentary mass to be between 5e10^{22} and 5e10^{23} g, which, assuming an average density of 2,000 kg m^{-3} (see below), corresponds to a global average thickness of 0.17–1.7 km. In several locations, sedimentary rock thicknesses are known to be very much greater. For example, the sedimentary sequence in Gale crater is measured to be 5 km (Grotzinger et al., 2015), the sedimentary sequence in Juventae Chasma (Valles Marineris) may be on the order of 3–6 km thick (Grotzinger & Milliken, 2012), and the Medusae Fossae Formation in places is up to 3 km thick (Bradley et al., 2002). Globally, the Martian sedimentary rock record is lithologically and mineralogically complex and influenced by a variety of sedimentary processes (e.g., chemical weathering, mineral sorting) and diagenetic processes (e.g., cementation, compaction, secondary porosity formation) (McLennan & Grotzinger, 2008; McLennan et al., 2019).

Although sedimentary rocks can contain large amounts of primary intergranular porosity, in many cases that porosity may be lost during compaction and/or filled by diagenetic cements during the lithification process (Boggs, 2009), and for Mars, such cements can be highly variable with respect to mineralogy (phyllosilicates, sulfates and chlorides of variable hydration state, amorphous silica and other amorphous, commonly hydrated, phases) (McLennan & Grotzinger, 2008; McLennan et al., 2019). Although such cements eliminate porosity, their densities can be significantly lower than the grain density of the clastic particles and so the overall effects on both bulk density and seismic velocities would be to lower them but it is not possible to make quantitative predictions.

There have been some attempts to independently constrain the densities of Martian sedimentary rocks. Using combined gravity and topography signatures, Ojha and Lewis (2018) estimated a bulk density of 1,765 ± 105 kg m^{-3} for the Medusae Fossae Formation (also see Watters et al., 2007), a notably low value that was attributed to the result from either high contents of water ice (Watters et al., 2007) or, more likely, elevated porosity (>35% averaged over 1.5 km depth) (Ojha & Lewis, 2018). Using the Curiosity rover accelerometer to measure the gravity field (Lewis et al., 2019), and correcting for the gravity field resulting from the Gale impact, Johnson et al. (2021) estimated the mean bulk density of the sedimentary rocks in Gale crater to be 2,300 ± 130 kg m^{-3}. This density was considered consistent with a porosity of 18 ± 6%, a value in turn consistent with lithified sedimentary rocks that have undergone about 4–5 km of burial compaction (Johnson et al., 2021).

Although considered less likely, another deep upper crustal lithology that may underlie the InSight landing site is aqueously altered Noachian igneous rocks, possibly similar to the rocks in the ancient highlands ∼500 km to the southwest. Pan et al. (2017) examined the mineralogy of deeper crustal materials exposed in craters throughout the northern lowland and found a variable mixture of primary volcanic mafic minerals and a variety of hydrous minerals, dominated by Fe/Mg phyllosilicates, interpreted to have formed by aqueous alteration processes in

the Noachian crust. The density of Fe/Mg phyllosilicates (e.g., nontronite, saponite) is mostly in the range of 2,200–2,300 kg m^{-3} (Anthony et al., 2002) and thus are also likely to lower the density of the primary crustal igneous materials.

4.2.3. Synthesis

From the above analysis, it is clear that porosity alone—in both sedimentary and volcanic rocks—could potentially explain the low average P-wave speed observed in Layer 1. On the other hand, it is less likely that lithological factors alone, such as the presence of cemented sedimentary rocks, aqueously altered igneous rocks, or more felsic rocks, could do so. Nevertheless, our current understanding suggests that the upper crustal stratigraphy beneath the landing site is dominated by lithologies that have reduced densities related to the presence of secondary materials such as sedimentary cements and other hydrous alteration phases. Accordingly, our favored hypothesis is that a combination of low-density lithologies (cemented sedimentary rocks, intermediate-felsic igneous rocks, and aqueously altered Noachian igneous rocks) almost certainly played a significant role in reducing P-wave speed. However, in addition to that, it is also necessary that significant primary porosity (and for sedimentary rocks, possibly secondary porosity) remained in many of these rocks.

A final issue is what is the origin of the seismic discontinuity at the base of Layer 1. Given the known thicknesses of sedimentary rocks on Mars, a Noachian sedimentary succession on the order of ≥7 km thickness is plausible and so one possibility is that the base of Layer 1 is essentially the base of a sedimentary rock sequence. If, on the other hand, aqueously altered igneous rocks dominate at these depths, then the boundary could also correspond to the maximum depth of aqueous alteration and therefore fluid flow.

In either case, it is likely that porosity also plays a significant role. Both compaction and viscous deformation will result in porosity reduction with depth. Gyalay et al. (2020) showed that the closure of pore space should occur over a narrow depth range of a few kilometers. Above this transition zone, the rocks retain their initial porosity, whereas below this transition zone all porosity is removed. The absolute depth of the transition zone depends upon the heat flow at the time when the porosity was created. If most porosities were created by impacts before 3.9 Ga, based on reasonable estimates of the surface heat flow at that time, all porosity would have since been removed for depths greater than about 12–23 km (Wieczorek et al., 2022). Thus, if Layer 1 initially contained high porosities near 22%–30% at 3.9 Ga, this porosity would remain to the present day. If Layer 1 instead formed at a later date (such as from sedimentary processes), these materials would also retain their initial porosity to the present day.

Accordingly, a combination of lithological change and pore reduction (or elimination) is a plausible mechanism to explain the seismic discontinuity at the base of Layer 1 and is also consistent with the known geological relationships in the vicinity of the InSight lander site.

5. Conclusions

We have analyzed one quality-A and five quality-B broadband and low-frequency events and made the first coherent detection of the SsPp phase on Mars, which helps us constrain the crustal structure at the lander site. We found that quality-B marsquakes, with simpler source wavelets, behave better than quality-A events when constraining the structure of the uppermost crustal layer (at about 8 km depth) when using the SsPp phase. We found coherent signals that are consistent with wave reflections off the first crustal interface, and this new phase confirms the existence of the ∼8 km interface in the crust and the large wave speed (or impedance) contrast across it. The detected SsPp phase helped reduce the number of acceptable models used in the previous receiver function analysis of Knapmeyer-Endrun et al. (2021) from 20,000 models to about 10,000 models.

Using our new constraint from the SsPp phase, we determined that the average P-wave speed in Layer 1 is between 2.5 km/s and 3.2 km/s, compared to the previous range of 2.0–3.5 km/s obtained by receiver function analysis. Based on these low average P-wave speeds, the seismic properties of Layer 1 likely result primarily from the presence of relatively low-density lithified sedimentary rocks and/or aqueously altered igneous rocks that also have a significant amount of porosity, possibly as much as ∼30% by volume.

Data Availability Statement

Data sets (both the raw data and the deglitched data in SAC format, after removing the instrument response) for this research are available on the Zenodo repository: https://doi.org/10.5281/zenodo.6784826.

References

Anthony, J. W., Bideaux, R. A., Bladh, K. W., & Nichols, M. C. (Eds.) (2002). *Handbook of mineralogy* (pp. 20151–1110). Mineralogical Society of America. Retrieved from http://www.handbookofmineralogy.org/

Banerdt, W. B., Smrekar, S. E., Banfield, D., Giardini, D., Golombek, M., Johnson, C. L., et al. (2020). Initial results from the InSight mission on Mars. *Nature Geoscience*, *13*(3), 183–189.

Besserer, J., Nimmo, F., Wieczorek, M. A., Weber, R. C., WalterKiefer, S., McGovern, P. J., et al. (2014). GRAIL gravity constraints on the vertical and lateral density structure of the lunar crust. *Geophysical Research Letters*, *41*(16), 5771–5777. https://doi.org/10.1002/2014gl060240

Beyreuther, M., Barsch, R., Krischer, L., Megies, T., Behr, Y., & Wassermann, J. (2010). ObsPy: A python toolbox for seismology. *Seismological Research Letters*, *81*(3), 530–533. https://doi.org/10.1785/gssrl.81.3.530

Boggs, S., Jr. (2009). *Petrology of sedimentary rocks*, 2nd ed. Cambridge University Press, (p. 600).

Bradley, B. A., Sakimoto, S. E., Frey, H., & Zimbelman, J. R. (2002). Medusae fossae formation: New perspectives from Mars global surveyor. *Journal of Geophysical Research*, *107*, E85050. https://doi.org/10.1029/2001JE001537

Brocher, T. M. (2005). Empirical relations between elastic wavespeeds and density in the earth's crust. *Bulletin of the Seismological Society of America*, *95*(6), 2081–2092. https://doi.org/10.1785/0120050077

Brown, G. C., & Mussett, A. E. (1993). The inaccessible earth: An integrated view of its structure and composition (p. 276).

Chen, Q., & Chen, W.-P. (2020). Toward simultaneous determination of bulk crustal properties using virtual deep seismic sounding. *Bulletin of the Seismological Society of America 110.3*, 1387–1392. https://doi.org/10.1785/0120190294

Chen, W. P., & Jiang, Y. (2020). Undulating moho beneath a near-uniform surface of central Tibet. *Earth and Planetary Science Letters*, *543*, 116343. https://doi.org/10.1016/j.epsl.2020.116343

Chen, W. P., Yu, C. Q., Tseng, T. L., Yang, Z., Wang, C. Y., Ning, J., & Leonard, T. (2013). Moho, seismogenesis, and rheology of the lithosphere. *Tectonophysics*, *609*, 491–503. https://doi.org/10.1016/j.tecto.2012.12.019

Christensen, N. I. (1972). Compressional and shear wave velocities at pressures to 10 kilobars for basalts from the east Pacific rise. *Geophysical Journal International*, *28*(5), 425–429. https://doi.org/10.1111/j.1365-246x.1972.tb06140.x

Christensen, N. I., & Salisbury, M. W. (1975). Structure and constitution of the lower oceanic crust. *Reviews of Geophysics and Space Physics*, *13*, 57–86. https://doi.org/10.1029/rg013i001p00057

Clinton, J. F., Ceylan, S., Van Driel, M., Giardini, D., Stähler, S. C., Böse, M., et al. (2021). The marsquake catalogue from InSight, sols 0–478. *Physics of the Earth and Planetary Interiors*, *310*, 106595. https://doi.org/10.1016/j.pepi.2020.106595

Coulson, I. M., Beech, M., & Nie, W. (2007). Physical properties of Martian meteorites: Porosity and density measurements. *Meteoritics & Planetary Sciences*, *42*, 2043–2054. https://doi.org/10.1111/j.1945-5100.2007.tb01006.x

Cousin, A., Sautter, V., Payré, V., Forni, O., Mangold, N., Gasnault, O., et al. (2017). Classification of igneous rocks analyzed by ChemCam at Gale crater. *Icarus*, *288*, 265–283. https://doi.org/10.1016/j.icarus.2017.01.014

Crameri, F. (2018). Scientific colour maps. *Zenodo*. https://doi.org/10.5281/zenodo.1243862

Cunningham, E., & Lekic, V. (2019). Constraining crustal structure in the presence of sediment: A multiple converted wave approach. *Geophysical Journal International*, *219*(1), 313–327. https://doi.org/10.1093/gji/ggz298

Deng, S., & Levander, A. (2020). Autocorrelation reflectivity of Mars. *Geophysical Research Letters*, *47*, e2020GL089630. https://doi.org/10.1029/2020gl089630

Drilleau, M., Samuel, H., Garcia, R., Rivoldini, A., Perrin, C., Michaut, C., et al. (2021). Marsquake locations and 1-D seismic models for Mars from InSight data. In Revision.

Durán, C., Khan, A., Ceylan, S., Zenhäusern, G., Stähler, S., Clinton, J. F., & Giardini, D. (2022). Seismology on Mars: An analysis of direct, reflected, and converted seismic body waves with implications for interior structure. *Physics of the Earth and Planetary Interiors*, *325*, 106851.

Förstner, U. (1967). Petrographische untersuchungen des suevit aus den bohrungen deiningen und wörnitzostheim im ries von nördlingen. *Contributions to Mineralogy and Petrology*, *15*, 281–308.

Gardner, G. H. F., Gardner, L. W., & Gregory, A. R. (1974). Formation velocity and density – The diagnostic basics for stratigraphic traps. *Geophysics*, *39*, 770–780. https://doi.org/10.1190/1.1440465

Golombek, M., Grott, M., Kargl, G., Andrade, J., Marshall, J., Warner, N., et al. (2018). Geology and physical properties investigations by the InSight lander. *Space Science Reviews*, *214*, 84. https://doi.org/10.1007/s11214-018-0512-7

Golombek, M., Kipp, D., Warner, N., Daubar, I. J., Fergason, R., Kirk, R. L., et al. (2017). Selection of the InSight landing site. *Space Science Reviews*, *211*, 5–95. https://doi.org/10.1007/s11214-016-0321-9

Golombek, M., Warner, N. H., Grant, J. A., Hauber, E., Ansan, V., Weitz, C. M., et al. (2020). Geology of the InSight landing site on Mars. *Nature Communications*, *11*, 1014.

Grotzinger, J. P., Gupta, S., Malin, M. C., Rubin, D. M., Schieber, J., Siebach, K., et al. (2015). Deposition, exhumation, and paleoclimate of an ancient lake deposit, Gale Crater, Mars. *Science*, *350*, aac7575. https://doi.org/10.1126/science.aac7575

Grotzinger, J. P., & Milliken, R. E. (2012). *The sedimentary rock record of Mars: Distribution, origins, and global stratigraphy*. In J. P. Grotzinger & R. E. Milliken (Eds.) (Vol. *102*, pp. 1–48). SEPM Special Publication. Mars Sedimentology. https://doi.org/10.2110/pec.12.102.0001

Gyalay, S., Nimmo, F., Plesa, A.-C., & Wieczorek, M. (2020). Constraints on thermal history of mars from depth of pore closure below InSight. *Geophysical Research Letters*, *47*, e2020Gl088653. https://doi.org/10.1029/2020gl088653

Heap, M. J. (2019). P-and S-wave velocity of dry, water-saturated, and frozen basalt: Implications for the interpretation of Martian seismic data. *Icarus*, *330*, 11–15. https://doi.org/10.1016/j.icarus.2019.04.020

Huang, Q., Schmerr, N. C., King, S. D., Kim, D., Rivoldini, A., Plesa, A. C., et al. (2022). Seismic detection of a deep mantle discontinuity within mars by InSight. *Proceedings of the National Academy of Sciences*, *119*(42), e2204474119. https://doi.org/10.1073/pnas.2204474119

Humayun, M., Nemchin, A., Zanda, B., Hewins, R. H., Grange, M., Kennedy, A., et al. (2013). Origin and age of the earliest Martian crust from meteorite NWA 7533. *Nature*, *503*, 513–516. https://doi.org/10.1038/nature12764

InSight Marsquake Service. (2020). Mars seismic catalogue, InSight mission; V1 2020-01-02.

InSight Marsquake Service. (2021a). Mars seismic catalogue, InSight mission; V8 2021-10-06.

InSight Marsquake Service. (2021b). Mars seismic catalogue, InSight mission; V7 2021-08-25.

InSight Marsquake Service. (2022a). Mars seismic catalogue, InSight mission; V10 upcoming.

InSight Marsquake Service. (2022b). Mars seismic catalogue, InSight mission; V9 upcoming.

InSight Mars SEIS Data Service. (2019). SEIS raw data, Insight Mission. IPGP, JPL, CNES, ETHZ, ICL, MPS, ISAE-Supaero.

InSight SEIS Data Bundle. (2021). PDS geosciences (GEO) node.

Johnson, B. C., Milliken, R. E., Lewis, K. W., & Collins, G. S. (2021). Impact generated porosity in gale crater and implications for the density of sedimentary rocks in lower Aeolis Mons. *Icarus*, *366*, 114539. https://doi.org/10.1016/j.icarus.2021.114539

Kang, D., Yu, C., Ning, J., & Chen, W. P. (2016). Simultaneous determination of crustal thickness and P wavespeed by virtual deep seismic sounding (VDSS). *Seismological Research Letters*, *87*(5), 1104–1111. https://doi.org/10.1785/0220160056

Kennett, B. L. N. (1991). The removal of free surface interactions from three-component seismograms. *Geophysical Journal International*, *104*(1), 153–154. https://doi.org/10.1111/j.1365-246x.1991.tb02501.x

Kennett, B. L. N. (2009). *Seismic wave propagation in stratified media*. ANU Press.

Kennett, B. L. N., & Engdahl, E. R. (1991). Traveltimes for global earthquake location and phase identification. *Geophysical Journal International*, *105*(2), 429–465. https://doi.org/10.1111/j.1365-246x.1991.tb06724.x

Khan, A., Ceylan, S., Van Driel, M., Giardini, D., Lognonné, P., Samuel, H., et al. (2021). Upper mantle structure of Mars from InSight seismic data. *Science*, *373*(6553), 434–438. https://doi.org/10.1126/science.abf2966

Kiefer, W. S., Macke, R. J., Britt, D. T., Irving, A. J., & Consolmagno, G. J. (2012). The density and porosity of lunar rocks. *Geophysical Research Letters*, *39*, 7. https://doi.org/10.1029/2012gl051319

Kim, D., Davis, P., Lekić, V., Maguire, R., Compaire, N., Schimmel, M., et al. (2021). Potential pitfalls in the analysis and structural interpretation of seismic data from the Mars InSight mission. *Bulletin of the Seismological Society of America*, *111*(6), 2982–3002. https://doi.org/10.1785/0120210123

Kim, D., Lekić, V., Irving, J. C. E., Schmerr, N., Knapmeyer-Endrun, B., Joshi, R., et al. (2021). Improving constraints on planetary interiors with PPS receiver functions. *Journal of Geophysical Research: Planets*, *126*(11), e2021JE006983. https://doi.org/10.1029/2021je006983

Knapmeyer-Endrun, B., Panning, M. P., Bissig, F., Joshi, R., Khan, A., Kim, D., et al. (2021). Thickness and structure of the martian crust from InSight seismic data. *Science*, *373*(6553), 438–443. https://doi.org/10.1126/science.abf8966

Laske, G., Masters, G., Ma, Z., & Pasyanos, M. (2013). Update on CRUST1. 0—A 1-degree global model of earth's crust. *Geophysical Research Abstracts*, *15*, 2658.

Lesage, P., Heap, M. J., & Kushnir, A. (2018). A generic model for the shallow velocity structure of volcanoes. *Journal of Volcanology and Geothermal Research*, *356*, 114–126. https://doi.org/10.1016/j.jvolgeores.2018.03.003

Lewis, K. W., Peters, S., Gonter, K., Morrison, S., Schmerr, N., Vasavade, A. R., & Gabriel, T. (2019). A surface gravity traverse on mars indicates low bedrock density at gale crater. *Science*, *363*, 535–537. https://doi.org/10.1126/science.aat0738

Li, J., Beghein, C., Davis, P., Lognonné, P., & Banerdt, W. B. (2022). Data for "crustal structure constraints from the detection of the SsPp phase on mars". *Zenodo*. https://doi.org/10.5281/ZENODO.6784826

Li, J., Beghein, C., Wookey, J., Davis, P., Lognonné, P., Schimmel, M., et al. (2022). Evidence for crustal seismic anisotropy at the InSight lander site. *Earth and Planetary Science Letters*, *593*, 117654. https://doi.org/10.1016/j.epsl.2022.117654

Liu, T., Klemperer, S. L., Gabriel, F., & Yu, C. (2019). Post-critical SsPmp and its applications to virtual deep seismic sounding (VDSS)–2: 1-D imaging of the crust/mantle and joint constraints with receiver functions. *Geophysical Journal International*, *219*(2), 1334–1347. https://doi.org/10.1093/gji/ggz370

Lognonné, P., Banerdt, W., Pike, W., Giardini, D., Christensen, U., Garcia, R. F., et al. (2020). Constraints on the shallow elastic and anelastic structure of mars from InSight seismic data. *Nature Geoscience*, *13*(3), 213–220.

Lognonne, P., Banerdt, W. B., Giardini, D., Panning, M., Pike, W. T., Barkaoui, S., et al. (2022). SEIS achievement for mars seismology after 1000 sols of seismic monitoring. *LPI Contribution*, *2678*, 2279.

Lognonné, P., Banerdt, W. B., Giardini, D., Pike, W. T., Christensen, U., Laudet, P., et al. (2019). SEIS: Insight's seismic experiment for internal structure of Mars. *Space Science Reviews*, *215*(1).

Manga, M., & Wright, V. (2021). No cryosphere-confined aquifer below InSight on mars. *Geophysical Research Letters*, *48*(8), e2021GL093127. https://doi.org/10.1029/2021gl093127

McLennan, S. M. (2012). Geochemistry of sedimentary processes on Mars. In J. P. Grotzinger & R. E. Milliken (Eds.) *Mars sedimentology* (Vol. 102, pp. 119–138). SEPM Special Publication. https://doi.org/10.2110/pec.12.102.0119

McLennan, S. M., & Grotzinger, J. P. (2008). The sedimentary rock cycle of mars. In J. F. Bell III (Ed.), *The Martian surface: Composition, mineralogy, and physical properties* (pp. 541–577). Cambridge University Press. https://doi.org/10.1017/cbo9780511536076.025

McLennan, S. M., Grotzinger, J. P., Hurowitz, J. A., & Tosca, N. J. (2019). The sedimentary cycle on early mars. *Annual Review of Earth and Planetary Sciences*, *166*, 110–130. https://doi.org/10.1146/annurev-earth-053018-060332

McSween, H. Y., Jr., Taylor, G. J., & Wyatt, M. B. (2009). Elemental composition of the Martian crust. *science*, *324*(5928), 736–739. https://doi.org/10.1126/science.1165871

Milbury, C., Johnson, B. C., Melosh, H. J., Collins, G. S., Blair, D. M., Soderblom, J. M., et al. (2015). Preimpact porosity controls the gravity signature of lunar craters. *Geophysical Research Letters*, *42*(22), 9711–9716. https://doi.org/10.1002/2015gl066198

Ojha, L., & Lewis, K. (2018). The density of the medusae fossae formation: Implications for its composition, origin, and importance in martian history. *Journal of Geophysical Research: Planets*, *123*, 1368–1379. https://doi.org/10.1029/2018je005565

Owens, T. J., & Zandt, G. (1997). Implications of crustal property variations for models of Tibetan plateau evolution. *Nature*, *387*(6628), 37–43. https://doi.org/10.1038/387037a0

Pan, L., Ehlmann, B. L., Carter, J., & Ernst, C. M. (2017). The stratigraphy and history of Mars' northern lowlands through mineralogy of impact craters: A comprehensive survey. *Journal of Geophysical Research: Planets*, *122*, 1824–1854. https://doi.org/10.1002/2017je005276

Pan, L., Quantin-Nataf, C., Tauzin, B., Michaut, C., Golombek, M., Lognonné, P., et al. (2020). Crust stratigraphy and heterogeneities of the first kilometers at the dichotomy boundary in western Elysium Planitia and implications for InSight lander. *Icarus*, *338*, 113511. https://doi.org/10.1016/j.icarus.2019.113511

Rae, A. S., Collins, G. S., Morgan, J. V., Salge, T., Christeson, G. L., Leung, J., et al. (2019). Impact-induced porosity and microfracturing at the chicxulub impact structure. *Journal of Geophysical Research: Planets*, *124*(7), 1960–1978. https://doi.org/10.1029/2019je005929

Schimmel, M., Stutzmann, E., Lognonné, P., Compaire, N., Davis, P., Drilleau, M., et al. (2021). Seismic noise autocorrelations on mars. *Earth and Space Science*, e2021EA001755. https://doi.org/10.1029/2021ea001755

Scholz, J.-R., Widmer-Schnidrig, R., Davis, P., Lognonné, P., Pinot, B., Garcia, R. F., et al. (2020). Detection, analysis, and removal of glitches from insight's seismic data from mars. *Earth and Space Science*, *7*(11), e2020EA001317. https://doi.org/10.1029/2020ea001317

Smith, D. E., Zuber, M. T., Frey, H. V., Garvin, J. B., Head, J. W., Muhleman, D. O., et al. (2001). Mars orbiter laser altimeter: Experiment summary after the first year of global mapping of mars. *Journal of Geophysical Research*, *106*(E10), 23689–23722. https://doi.org/10.1029/2000je001364

Soderblom, J. M., Evans, A. J., Johnson, B. C., Melosh, H. J., Miljković, K., Phillips, R. J., et al. (2015). The fractured moon: Production and saturation of porosity in the lunar highlands from impact cratering. *Geophysical Research Letters*, *42*(17), 6939–6944. https://doi.org/10.1002/2015gl065022

Stähler, S. C., Khan, A., Banerdt, W. B., Lognonné, P., Giardini, D., Ceylan, S., et al. (2021). Seismic detection of the martian core. *Science*, *373*(6553), 443–448.

Taylor, S. R., & McLennan, S. M. (2009). *Planetary crusts: Their composition, origin and evolution* (p. 378). Cambridge University Press.

Toksöz, M. N., Cheng, C. H., & Timur, A. (1976). Velocities of seismic waves in porous rocks. *Geophysics*, *41*(4), 621–645.

Tseng, T. L., Chen, W. P., & Nowack, R. L. (2009). Northward thinning of Tibetan crust revealed by virtual seismic profiles. *Geophysics Research Letters*. https://doi.org/10.1029/2009gl040457

Warner, N. H., Golombek, M. P., Ansan, V., Marteau, E., Williams, N., Grant, J. A., et al. (2022). In situ and orbital stratigraphic characterization of the insight landing site – a type example of a regolith-covered lava plain on Mars. *Journal of Geophysical Research: Planets*, *127*, e2022JE007232. https://doi.org/10.1029/2022je007232

Watters, T. R., Campbell, B., Carter, L., Leuschen, C. J., Plaut, J. J., Picardi, G., et al. (2007). Radar sounding of the medusae fossae formation mars: Equatorial ice or dry, low density deposits? *Science*, *318*, 1125–1128. https://doi.org/10.1126/science.1148112

Wieczorek, M. A., Broquet, A., McLennan, S. M., Rivoldini, A., Golombek, M., Antonangeli, D., et al. (2022). InSight constraints on the global character of the Martian crust. *Journal of Geophysical Research: Planets*, e2022JE007298. https://doi.org/10.1029/2022je007298

Wieczorek, M. A., Neumann, G. A., Nimmo, F., WalterKiefer, S., Taylor, G. J., Melosh, H. J., et al. (2013). The crust of the moon as seen by GRAIL. *Science*, *339*, 671–675. https://doi.org/10.1126/science.1231530

Yu, C., Chen, W. P., & Van der Hilst, R. D. (2016). Constraints on residual topography and crustal properties in the western United States from virtual deep seismic sounding. *Journal of Geophysical Research: Solid Earth*, *121*(8), 5917–5930. https://doi.org/10.1002/2016jb013046

Yu, C., Zheng, Y., & Shang, X. (2017). Crazyseismic: A MATLAB GUI-based software package for passive seismic data preprocessing. *Seismological Research Letters*, *88*(2A), 410–415. https://doi.org/10.1785/0220160207

Yu, C. Q., Chen, W. P., Ning, J. Y., Tao, K., Tseng, T. L., Fang, X. D., et al. (2012). Thick crust beneath the Ordos plateau: Implications for instability of the north China craton. *Earth and Planetary Science Letters*, *357*, 366–375. https://doi.org/10.1016/j.epsl.2012.09.027

Yu, C. Q., Chen, W. P., & Van der Hilst, R. D. (2013). Removing source-side scattering for virtual deep seismic sounding (VDSS). *Geophysical Journal International*, *195*(3), 1932–1941. https://doi.org/10.1093/gji/ggt359

Zandt, G., & Randall, G. E. (1985). Observations of shear-coupled P waves. *Geophysical Research Letters*, *12*(9), 565–568. https://doi.org/10.1029/gl012i009p00565

Zenhäusern, G., Stähler, S. C., Clinton, J. F., Giardini, D., Ceylan, S., & Garcia, R. F. (2022). *Low-frequency marsquakes and where to find them: Back azimuth determination using a polarization analysis approach*. Bulletin of the Seismological Society of America.

Zhou, L., Chen, W. P., & Ozalaybey, S. (2000). Seismic properties of the central Indian shield. *Bulletin of the Seismological Society of America*, *90*(5), 1295–1304. https://doi.org/10.1785/0119990039

References From the Supporting Information

Compaire, N., Margerin, L., Garcia, R. F., Pinot, B., Calvet, M., Orhand-Mainsant, G., et al. (2021). Autocorrelation of the ground vibrations recorded by the seis-insight seismometer on Mars. *Journal of Geophysical Research: Planets*, *126*(4), e2020JE006498. https://doi.org/10.1029/2020je006498

Wang, R. (1999). A simple orthonormalization method for stable and efficient computation of green's functions. *Bulletin of the Seismological Society of America*, *89*(3), 733–741.